
# Atmospheric parameters and chemical abundances of young stars with APOGEE – I. Orion star-forming region

Monthly Notices of the ROYAL ASTRONOMICAL SOCIETY

MNRAS **543,** 420–434 (2025)
Advance Access publication 2025 September 01

https://doi.org/10.1093/mnras/staf1445

# Atmospheric parameters and chemical abundances of young stars with APOGEE – I. Orion star-forming region

Ricardo López-Valdivia [1]★ Lucía Adame,[1] Carlos G. Román-Zúñiga [1] Jesús Hernández,[1] Edilberto Sánchez,[1] Itzarel Herrnández-Aburto,[1] José G. Fernández-Trincado [2] Eduardo Zagala Lagunas,[3] Leticia Carigi [4] J. E. Méndez-Delgado [4] Marina Kounkel [5] Javier Serna [6] Richard R. Lane,[7] Keivan G. Stassun [8] Sandro Villanova,[9] Jinyoung Serena Kim,[10] S. J. Wolk,[11] Guy S. Stringfellow [12] Jonathan C. Tan,[13,14] A. Roman-Lopes,[15] Bárbara Rojas-Ayala [16] and Rakesh Pandey[17]

*Affiliations are listed at the end of the paper*

Accepted 2025 August 26. Received 2025 August 12; in original form 2025 June 7

## ABSTRACT

We derive atmospheric parameters and chemical abundances in young G-, K-, and M-type stars (temperatures between 6500 and 3100 K) using infrared APOGEE-2 spectra. Atmospheric parameters were determined for 548 young stars in the Orion complex (Orion A, B, OB1, and λ Ori) using the TONALLI code. For 340 slow rotators ($v \sin i \leq 30$ km s$^{-1}$), we derived C, Mg, Si, K, Ti, and Fe abundances using 19 atomic lines, MARCS model atmospheres, and BACCHUS. To mitigate the impact of circumstellar material, we excluded stars with infrared excess identified via 2MASS and *WISE* photometry. We find subsolar [X/H] abundance ratios, consistent across elements and among all four groups, suggesting a chemically homogeneous Orion complex. We computed [$\alpha$/Fe] from [Mg/Fe], [Si/Fe], and [Ti/Fe], obtaining a median of $-0.14 \pm 0.04$, about 0.10 dex lower than the value for nearby main-sequence stars ($-0.04 \pm 0.04$) at similar [Fe/H]. This result aligns with predictions from Galactic chemical evolution models. Furthermore, the median [C/H] abundance we derived for Orion agrees with previous estimations based on the analysis of the ionized gas of the Orion nebula. This work sets the stage for extending the analysis to stars with circumstellar material and higher rotational velocities, which will not only improve our understanding of Orion, but also provide critical insight into the formation and evolution of young stars, as well as the chemical evolution of the Milky Way.

**Key words:** stars: abundances – stars: fundamental parameters – stars: pre-main-sequence – infrared: stars.

## 1 INTRODUCTION

In recent years, thanks to large-area spectroscopic surveys like the RAdial Velocity Experiment (RAVE; Steinmetz 2003; Guiglion et al. 2020), the Large Sky Area Multi-Object Fiber Spectroscopic Telescope (LAMOST; Cui et al. 2012; Zhao et al. 2012), the *Gaia*-ESO (Gilmore et al. 2012), the GALactic Archeology with Hermes (GALAH; De Silva et al. 2015; Martell et al. 2017), and the Sloan Digital Sky Survey IV (SDSS-IV; Blanton et al. 2017) APOGEE-2 (Majewski et al. 2017) and SDSS-V (Almeida et al. 2023) Milky Way Mapper (Kollmeier et al. 2017), we have access to enormous inventories of stellar spectra with diverse stellar populations. These and other surveys are designed to provide uniform quality data, with sufficient signal-to-noise ratio (SNR) and spectral resolution to allow us the extraction of reliable stellar parameters, like effective temperature ($T_{eff}$), surface gravity (log g), overall metallicity ([M/H]), age, and mass.

The core samples of most of the mentioned surveys were stars in the main sequence or post-main-sequence, with relatively quiescent photospheres that allow comparing properties of stellar populations in distinct Galactic components. However, pre-main sequence or very young stars (age $<$ 300 Myr) are subject to various processes that complicate the determination of their properties directly from their spectra, like high stellar rotation, magnetic activity, and variability.

The SDSS-IV APOGEE-2 survey, which operates in the *H* band (∼1.5–1.7μm), provides a valuable window into the stellar photospheres of young stars. This wavelength range is significantly less affected by interstellar extinction and continuum veiling than the optical regime, making it especially suitable for studying recently formed stars in nearby star-forming regions. Consequently, APOGEE-2 data has become an increasingly used tool in the investigation of young stellar populations (e.g. Cottaar et al. 2014, 2015; Foster et al. 2015; Fernandez et al. 2017; Roman-Lopes et al. 2019; Román-Zúñiga et al. 2023). However, a persistent challenge remains: the reliable ($\sigma \lesssim 0.1$ dex) determination of chemical abundances in young stars. Although early studies (e.g. Padgett 1996; Santos et al. 2008) achieved abundance uncertainties slightly above 0.1 dex, they

★ E-mail: rlopezv@astro.unam.mx

were limited by small sample sizes, which prevented more detailed chemical analyses.

The Orion star-forming region, one of the most studied regions due to its youth and number of stars (e.g. Blaauw 1964; Brown, Hartmann & Burton 1995; Stassun et al. 1999; Da Rio et al. 2016, 2017; Kounkel et al. 2018; Hernández et al. 2023) has been the focus of ongoing debate regarding its chemical homogeneity. The answer to this debate is of particular interest in better understanding and constraining models of the chemical evolution of star-forming regions. The topic is still open. For example, Cunha & Lambert (1994) determined the abundance of C, N, O, Si, and Fe for 18 B-type main-sequence stars located in four groups of different ages. They found that the abundance of O and Si was higher, up to 40 per cent, in some of the youngest stars analysed, but found no enrichment in C, N, or Fe. The authors suggested that the observed trend to the enrichment of the molecular cloud (where such stars formed) with the ejecta material of type II supernovae, which is rich in O and Si but not in C or N. Cunha, Smith & Lambert (1998) found a similar trend in F and G Orion stars. In contrast, Simón-Díaz (2010) showed that the Si and O abundances of B stars in four subgroups of Orion OB1 were all consistent with solar values. Later, D'Orazi et al. (2009) found that stars in the Orion OB1 group show a lower Fe abundance value than younger, more embedded regions like the Orion nebula cluster. Subsequent studies of Biazzo et al. (2011, 2012) confirmed, through the abundance analysis of several elements, that Orion is consistent with a thin-disc population.

More recently, Kos et al. (2021) revisited the chemical inhomogeneity in Orion using a significantly larger sample of GALAH spectra, consisting of about 300 stars across 15 different stellar clusters. Their results showed no evidence of self-enrichment in the λ-Ori group relative to the Orion B and Orion OB groups, suggesting that the Orion complex is chemically homogeneous. It is important to note that Kos et al. (2021) reported strong correlations between elemental abundances and $T_{\rm eff}$, similar to those found by Viana Almeida et al. (2009) for Fe. These trends may indicate unaccounted factors such as stellar variability, departures from Local Thermodynamic Equilibrium (LTE), model dependencies, inaccurate atomic data, and line blending.

The present study aims to present the chemical abundances of young stars in four different groups of Orion through a homogeneous and consistent method. We take advantage of the quantity and quality of the near-infrared spectra of the SDSS-IV APOGEE-2 survey, and our goal is to contribute to the understanding of the chemical evolution of star-forming regions.

## 2 ORION SAMPLE

Román-Zúñiga et al. (2023) presented a catalogue consisting of 3360 young stars, ranging from subsolar to supersolar spectral types, located in 16 Galactic star-forming regions and young open clusters observed by the APOGEE-2 survey (Majewski et al. 2017). Román-Zúñiga et al. (2023) selected the young stars in this catalogue using a clustering method that removed most field contamination, yielding a robust sample of bona fide members of their respective star-forming regions.

To define our working sample, we retrieved all epoch-combined 1D infrared spectra of the 1861 Orion members identified by Román-Zúñiga et al. (2023) from the APOGEE-2 DR17 public database.[1]

[1]We used the apStar spectra downloaded from the SDSS-IV science archive webapp.

Young stars often exhibit infrared excesses caused by interstellar extinction or the presence of a protostellar disc. Both extinction and disc-related phenomena relate to additional physical processes, including accretion, magnetic activity, and continuum veiling, that can significantly affect the determination of atmospheric parameters and chemical abundances. For instance, continuum veiling is a non-stellar emission that reduces the depth of photospheric absorption lines in the spectra of young stars (Joy 1949). In the infrared, veiling is attributed to excess emission from dust at the inner disc wall's sublimation radius (e.g. Natta et al. 2001; Muzerolle et al. 2003) and to warm gas within that radius (e.g. Fischer et al. 2011).

Determining the veiling is a complex task that lies beyond the scope of this paper. However, we minimized its impact by identifying and excluding from our sample those stars exhibiting infrared excess, following a semi-empirical approach. We collected Two Micron All-Sky Survey (2MASS) and *Wide-field Infrared Survey Explorer (WISE)* photometry for a sample of main-sequence stars brighter than $J < 13$. The sample was divided into 15 bins of $J$-band magnitude, and a Gaussian function was fitted to the corresponding $(K - W3)$ colour distributions to determine their expected photospheric flux values. The results showed that, for bright stars ($J < 8$ mag), the photospheric flux remains approximately constant at 0.267 mag. For stars in the range $8 < J < 13$, the photospheric flux is better described by the following fourth-degree polynomial:

$$(K - W3)_{\rm phot} = a + bJ + cJ^2 + dJ^3 + eJ^4, \quad (1)$$

where $a = 0.5138$, $b = -0.2258$, $c = 0.0713$, $d = -0.0091$, and $e = 0.0004$. We looked for the 2MASS (Cutri et al. 2003) and *WISE* (Wright et al. 2010) photometry for the young stars of Orion in the ALLWISE catalogue (Cutri et al. 2013). The ALLWISE catalogue provides the *WISE* photometry quality and contamination flags, which are useful to identify bad *WISE* data. The quality flag (qph) measures the quality of the profile fit photometry, based on the SNR of each band, while the contamination flag (ccf) indicates if the photometry may be affected by an image artefact. We found that 559 sources had reliable (qph equal to A, B, or C) and unaffected (ccf = 0) *WISE* photometry and $(K - W3)$ consistent, within 1.5 times their respective error, with their corresponding photospheric value. These stars comprised our final working sample.

Most of our young stars are in the Orion OB1 group (228 stars). The remaining stars are located mostly uniformly in the λ Ori (116), Orion A (112), and Orion B (103) groups. The spatial distribution of our young sample is presented in Fig. 1.

## 3 ATMOSPHERIC PARAMETER DETERMINATION

In this section, we summarize the methods followed to determine the atmospheric parameters of the Orion stars. We recommend the reader see a more detailed explanation about TONALLI in Adame et al. (2024) and on using TONALLI in a stellar sample of low-mass main-sequence stars in López-Valdivia et al. (2024).

### 3.1 TONALLI

To determine the basic atmospheric parameters of our sample, we employed the code TONALLI (Adame et al. 2024).

In short, TONALLI, which is based on the Asexual Genetic Algorithm of Cantó, Curiel & Martínez-Gómez (2009), randomly selects a set of stellar parameters and interpolates a synthetic spectrum at those values using the synthetic spectral grid of Jönsson et al. (2020). The resulting synthetic spectrum is then rotationally broadened using

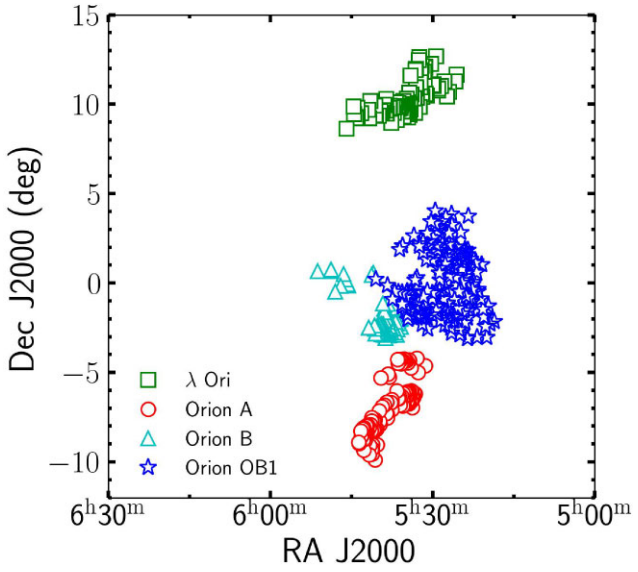


**Figure 1.** Spatial distribution of the 559 young stars located in the Orion star-forming region analysed in this work.

the kernel described by Gray (2008), assuming a limb darkening coefficient of 0.4. Finally, it is compared with the observed spectrum using a $\chi^2$ statistic. The stellar parameters (including $v \sin i$) that produce the lower $\chi^2$ values are selected as 'fathers' to create the next generation of synthetic spectra. In the next generation, the synthetic spectra are created by randomly selecting spectra from a small vicinity around each father, and these new synthetic spectra are compared again to the observed spectrum, finding new fathers. The search vicinity around the fathers decreases in size each generation until the stop criteria are achieved and the best-fitting spectrum is found.

The atmospheric parameters fitted by TONALLI are variable, and they are directly related to the theoretical grid used. In our case, we fitted the effective temperature ($T_{\rm eff}$), surface gravity ($\log g$), overall metallicity ([M/H])[2], $\alpha$-elements enhancement, and the projected rotational velocity ($v \sin i$). The first four atmospheric parameters are bounded by the limits of the Jönsson et al. (2020) grid, while the allowed range for $v \sin i$ is set by the user.

It is important to note that Jönsson et al. (2020) specifically developed a set of synthetic spectral grids tailored for APOGEE data. These grids are based on MARCS model atmospheres (Gustafsson et al. 2008), match the average spectral resolution of APOGEE observations, and are synthesized at five different microturbulence velocities ($\xi$). For our analysis, we used the grid computed at $\xi = 2.4$ km s$^{-1}$ and explored the full parameter space coverage for $T_{\rm eff}$, [M/H], and [$\alpha$/Fe] (see Table 1). For the $v \sin i$, we constrained our fitting procedure to $v \sin i$ values between 0 and 50 km s$^{-1}$. Although pre-main-sequence stars might have rotational velocities higher than 50 km s$^{-1}$, their atmospheric parameters and chemical abundance determinations become more challenging due to the line blending produced in the spectrum by the rotation.

Regarding $\log g$, we used TEPITZIN, a photometric module incorporated in the TONALLI ecosystem, to obtain a photometric $\log g$ value that could be used as a prior (Adame et al., in preparation). TEPITZIN minimizes the distances between the observed photometric colours (2MASS and *Gaia*) and the theoretical ones of the PARSEC

[2]This value comprises the sum of all metals.

**Table 1.** Parameter space of the MARCS synthetic grid used in this work.

| Parameter | Range | Step |
|---|---|---|
| $T_{\rm eff}$ | 3000–8000 K | 100 K for $T_{\rm eff} \leq 4000$ K<br>250 K otherwise |
| log g | 0.0–5.5 dex | 0.5 dex |
| [M/H] | −2.50–1.00 dex | 0.25 dex |
| [$\alpha$/Fe] | −0.75–1.00 dex | 0.25 dex |

pre-main-sequence evolutionary models (Marigo et al. 2017) to determine a best-fitting photometric $\log g$ value. This photometric $\log g$ value serves as the centre of a prior that is given to TONALLI. To keep consistent with the rest of the atmospheric parameters, we used a flat prior of 1 dex of total width, however, the user could choose a Gaussian or other functional form for this prior.

Most of the young stars of Orion might still be, at least partially, embedded into their progenitor cloud producing a reddening that affects their photometry. Reddening would lead to inaccurate $\log g$ photometric values. For this reason, it is necessary to correct the photometry of our sample before using it in TEPITZIN.

To determine the visual extinction ($A_v$) of our sample, we implemented the code MASSAGE (Hernández et al. 2023). MASSAGE requires temperature, *Gaia* (Gp, Rp, and Bp), and 2MASS (J and H) photometry to compute $A_v$ by minimizing the differences between the observed and expected intrinsic colours of Marigo et al. (2017) affected by reddening. The extinction $A_v$ is changed until the best comparison is found through a $\chi^2$ statistic. We determined $A_v$ for our sample, de-reddened their photometry, and then used the extinction corrected photometry into TEPITZIN to obtain a prior on $\log g$.

### 3.2 Atmospheric parameters

Once we have the extinction corrected photometry, we determined the final atmospheric parameters (and their errors) of our sample performing 30 repetitions in TONALLI. We used the median (50 percentile) of the posterior distributions as the value of the parameter analysed. We took the interquartile range of the results as the associated error[3] to each parameter.

We discarded from our analysis five stars as their interquartile range in $T_{\rm eff}$ is higher than 500 K and six more with interquartile range in $v \sin i$ higher than 5 km s$^{-1}$, as we consider them inaccurate determinations. We report in Table 2 the atmospheric parameters found for the remaining 548 young stars of Orion. In Fig. 2, we show the Kiel diagram ($\log g$ versus $T_{\rm eff}$) for our sample. In general, the $T_{\rm eff}$ and $\log g$ values found with TONALLI lie in the expected range for young stellar objects as predicted by the evolutionary tracks of Marigo et al. (2017).

For most of the objects in our sample, we determined $T_{\rm eff}$ between 3200 and 6000 K, corresponding approximately to spectral types M5/M4 to F9 (e.g. Herczeg & Hillenbrand 2014), although we found some stars with temperatures as high as ∼6400 K. Adame et al. (2024) found that TONALLI is capable of recovering reliable atmospheric parameters for stars with $T_{\rm eff}$ below ∼6200 K. This behaviour is linked to the theoretical grid of Jönsson et al. (2020), as at higher $T_{\rm eff}$ the number of spectral features becomes scarcer, complicating the fitting process and increasing the sensitivity to grid degeneracies.

[3]The interquartile range is defined as the difference between the 75 and 25 percentiles of the posterior distribution.

**Table 2.** Descriptive content of the Table of the stellar parameters and chemical abundances determined in this work. The full table is available in the electronic version of the paper.

| Column name | Description |
|---|---|
| OBJ | 2MASS identification number |
| RA | Right ascension (J2000) |
| Dec | Declination (J2000) |
| t25 | Effective temperature at percentile 25 |
| t50 | Effective temperature at percentile 50 |
| t75 | Effective temperature at percentile 75 |
| g25 | Surface gravity at percentile 25 |
| g50 | Surface gravity at percentile 50 |
| g75 | Surface gravity at percentile 75 |
| m25 | Overall metallicity at percentile 25 |
| m50 | Overall metallicity at percentile 50 |
| m75 | Overall metallicity at percentile 75 |
| a25 | Alpha elements abundance at percentile 25 |
| a50 | Alpha elements abundance at percentile 50 |
| a75 | Alpha elements abundance at percentile 75 |
| v25 | Projected rotational velocity at percentile 25 |
| v50 | Projected rotational velocity at percentile 50 |
| v75 | Projected rotational velocity at percentile 75 |
| C_H | Mean [C/H] abundance |
| lowC | Lower error in carbon abundance |
| uppC | Upper error in carbon abundance |
| lC | Number of lines used in carbon abundance determination |
| Mg_H | Mean [Mg/H] abundance |
| lowMg | Lower error in magnesium abundance |
| uppMg | Upper error in magnesium abundance |
| lMg | Lines used in magnesium abundance determination |
| Si_H | Mean [Si/H] abundance |
| lowSiLLL | Lower error in silicon abundance |
| uppSi | Upper error in silicon abundance |
| lSi | Lines used in silicon abundance determination |
| K_H | Mean [K/H] abundance |
| lowK | Lower error in potassium abundance |
| uppK | Upper error in potassium abundance |
| lK | Lines used in potassium abundance determination |
| Ti_H | Mean [Ti/H] abundance |
| lowTi | Lower error in titanium abundance |
| uppTi | Upper error in titanium abundance |
| lTi | Lines used in titanium abundance determination |
| Fe_H | Mean [Fe/H] abundance |
| lowFe | Lower error in iron abundance |
| uppFe | Upper error in iron abundance |
| lFe | Lines used in iron abundance determination |
| vmic | Microturbulence velocity |
| alfa_Fe | Alpha-elements to iron abundance ratio |
| e_alfa_Fe | Error in alfa_Fe abundance |

Regarding log $g$, our estimates show a bimodal distribution, with peaks around ∼3.8 and ∼4.2 dex, spanning a total range from approximately 3.3 to 4.6 dex. This bimodality may reflect slight differences in stellar ages among the four Orion subgroups analysed, given that log $g$ serves as a proxy for stellar age.

The [M/H] values obtained with TONALLI for the Orion stars are centred at $-0.08 \pm 0.12$ dex, which is consistent with the solar metal content within the errors. On the other hand, we found a mean [$\alpha$/Fe] for our sample around $-0.03 \pm 0.06$ dex, which is a value also consistent with the solar value, and it is well below the grid step of 0.25 dex. The metallicity and $\alpha$-elements enhancement estimations are in agreement with recent determinations of Kos et al. (2021). However, these values should not be considered precise measurements; instead, they represent approximate global estimates from the synthetic models that best fit the observed spectra and are mainly suitable for first-order comparisons. To derive more accurate abundances, a detailed line-by-line analysis is necessary.

Finally, we identified that 73 per cent of our sample (402 stars) have projected rotational velocities ($v \sin i$) $\leq$ 35 km s$^{-1}$, with a mean value of 20 km s$^{-1}$. In contrast, a substantial subset of 98 stars exhibit $v \sin i$ values between 45 and 50 km s$^{-1}$. It is important to emphasize that atmospheric parameters for these high $v \sin i$ sources should be interpreted with extreme caution. First, edge effects may compromise the reliability of the results, as our analysis explores velocities only up to 50 km s$^{-1}$. For instance, if a star intrinsically rotates faster than this limit, TONALLI will be unable to adequately broaden the synthetic spectrum to match the observed line depths. As a result, the code compensates by adjusting other parameters, such as $T_{\rm eff}$, log $g$, or [M/H], in an attempt to reproduce shallower lines, which can lead to anomalous or unphysical values. This effect is not exclusive to $v \sin i$; it applies to all parameters. Once the algorithm reaches the edge of the parameter space in any dimension, it tends to compensate by aggressively modifying the remaining parameters, thereby introducing potential biases. As we show in the next section, we found that the most objects with $v \sin i$ between 45 and 50 km s$^{-1}$ exhibit artificially low [M/H] values. Secondly, increasing $v \sin i$ leads to significant line blending, which degrades our ability to accurately determine parameters, particularly those with subtler spectroscopic signatures, such as log $g$ and [M/H]. In these cases, our derived values should be considered as first-order approximations. In Fig. 3, we show a portion of the observed spectra overplotted with the corresponding best-fitting synthetic spectra for three different Orion stars. These stars have similar values of $T_{\rm eff}$, log $g$, [M/H], and [$\alpha$/Fe], but significantly different $v \sin i$ values, highlighting the challenges in characterizing fast rotators. The fits for the stars with moderate $v \sin i$ (upper and middle panels) show excellent agreement with the observations. In contrast, the star in the bottom panel, which has a higher rotational velocity, exhibits a noticeably poorer fit. This example illustrates how high rotation complicates spectral analysis and may lead to less reliable atmospheric parameters, particularly for log g and [M/H].

### 3.3 Comparing TONALLI parameters with literature

We compared our stellar parameters with those from three different studies: The APOGEE Stellar Parameters and Chemical Abundances Pipeline in its version corresponding to DR17 (ASPCAP DR17; Abdurro'uf et al. 2022), APOGEE Net III (ANet III; Sizemore et al. 2024), and *Gaia* DR3 (Gaia Collaboration 2023).

The ASPCAP Pipeline used a minimum $\chi^2$ statistic to compare observed APOGEE spectra to a set of model libraries in a two-step process that determined stellar parameters and abundances.

On the other hand, ANet III (Sizemore et al. 2024), and its predecessor (Olney et al. 2020; Sprague et al. 2022), used a deep convolutional neural network to predict $T_{\rm eff}$, log $g$, and [M/H] based on previously derived parameters (or 'labels') collected for APOGEE data and other stars in diverse studies.

Finally, the *Gaia* DR3 (Gaia Collaboration 2023) team estimated $T_{\rm eff}$, log $g$, [M/H], radius, absolute magnitude $G$, distance and line-of-sight extinction from low-resolution optical BP/RP spectra, apparent $G$ magnitude and parallax. They employed a Markov Chain Monte Carlo (MCMC) algorithm in three different steps to derive the

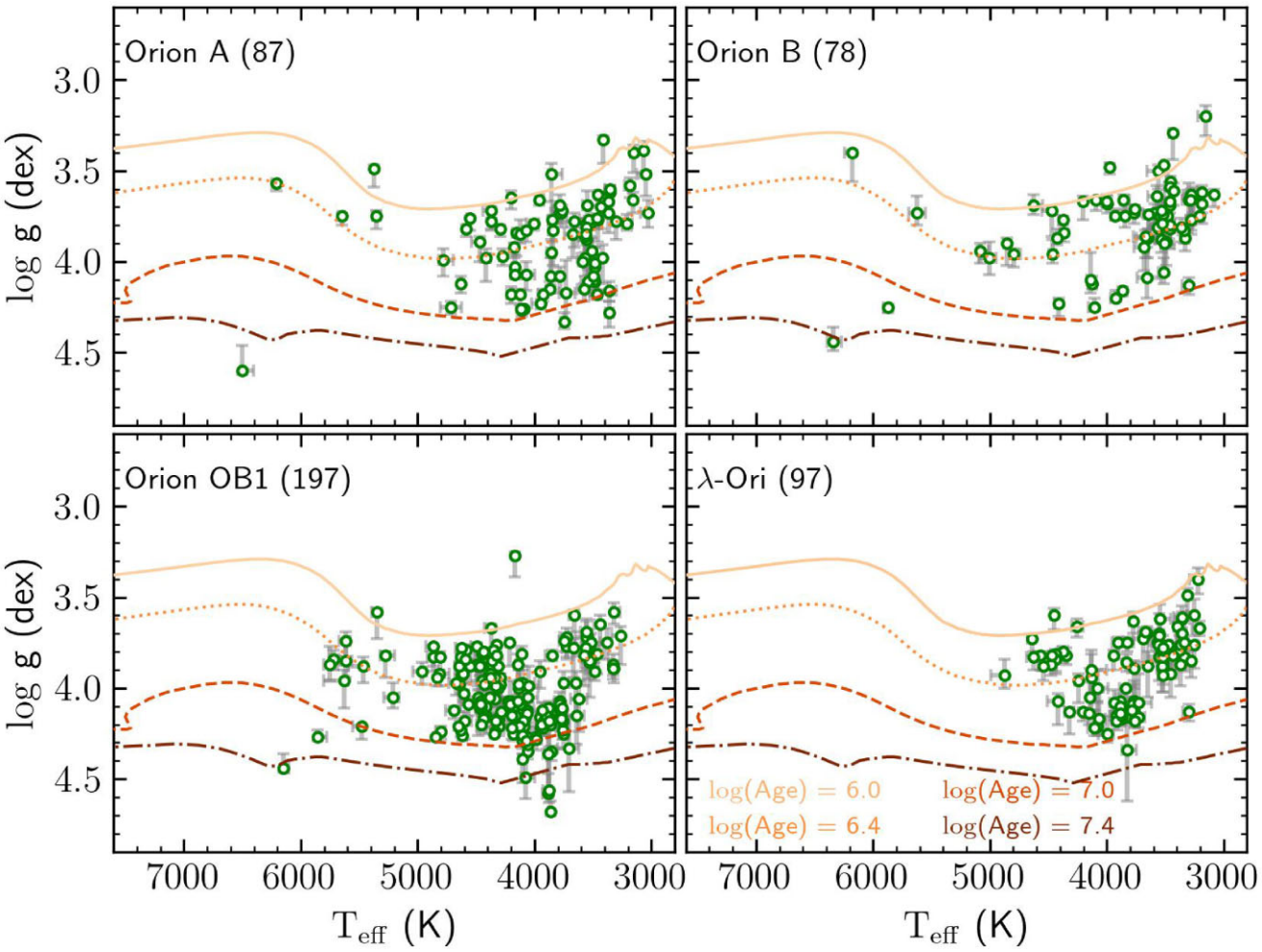


**Figure 2.** Kiel diagrams obtained with TONALLI for the 548 stars of Orion split into the four groups analysed. As a reference, we include, as colour lines, evolutionary models of Marigo et al. (2017) for solar metallicity at log(Age) = 6.0, 6.4, 6.8, and 7.2, corresponding roughly to 1, 2.5, 6.3, and 15 Myr, respectively. The numbers enclosed in the parentheses are the sources included in each stellar group.

parameters mentioned above in a self-consistent manner from four grids of synthetic spectra and a set of PARSEC COLIBRI isochrones (Tang et al. 2014; Chen et al. 2015; Pastorelli et al. 2020).

Among the three pipelines mentioned above, ANet III focuses more specifically on the characterization of young stars, producing parameters that are more adequate for a direct comparison with our work.

In Fig. 4, we compare our temperature estimates with the studies mentioned above. We have good agreement with ASPCAP DR17 and ANet III as we found a mean difference (literature – ours) of 62 ± 213 K and 92 ± 238 K, respectively. Both comparisons reveal a similar trend: hotter stars exhibit larger discrepancies between studies. This divergence becomes noticeable for sources with TONALLI $T_{\rm eff}$ above 5000 K, where the mean temperature difference reaches 190 ± 170 K and 290 ± 213 K for ASPCAP DR17 and ANet III, respectively. In contrast, for stars cooler than 5000 K, the differences are significantly smaller, just 37 ± 90 K and 66 ± 112 K. This behaviour may stem from the fact that hotter stars have fewer spectral features in the *H*-band, making temperature determinations more challenging. For TONALLI, temperature estimates become less reliable beyond ∼6000 K (López-Valdivia et al. 2024). The comparison with ASPCAP DR17 shows smaller discrepancies, likely due to the use of the same model atmospheres and observational data. Nevertheless, differences in continuum normalization and parameter determination methods may still introduce variations (though these remain within typical uncertainties). In contrast, ANet III relies on a machine learning approach based on the spectroscopic labels of its training set, which may introduce a systematic offset that contributes to the observed differences.

However, some *Gaia* DR3 temperatures are overestimated, in extreme cases up to 2000 K. This effect might be due to the degeneracy of the evolutionary tracks for giants and young stars used in the *Gaia* determination pipeline.

Regarding log *g*, we observe systematic trends in the residuals shown in Fig. 5. Across all three panels, the trend is consistent: at lower TONALLI log *g* values, literature estimates tend to be higher by up to 1.0 dex. This discrepancy decreases as log g approaches ∼4.1 dex, at which point the trend inverts, with TONALLI values becoming higher, up to 0.5 dex, than those reported in the literature. Surface gravity is arguably the most challenging atmospheric parameter to determine, as its influence on spectral lines overlaps with that of other parameters but with subtler effects. Notably, several ASPCAP DR17 log *g* values cluster at 4.5 dex, which appears slightly too high for young, low-mass stars. Notably, several ASPCAP DR17 log *g* values cluster near 4.5 dex, which would be too high for pre-main sequence stars; however, it is worth noticing that ASPCAP DR17 is optimized

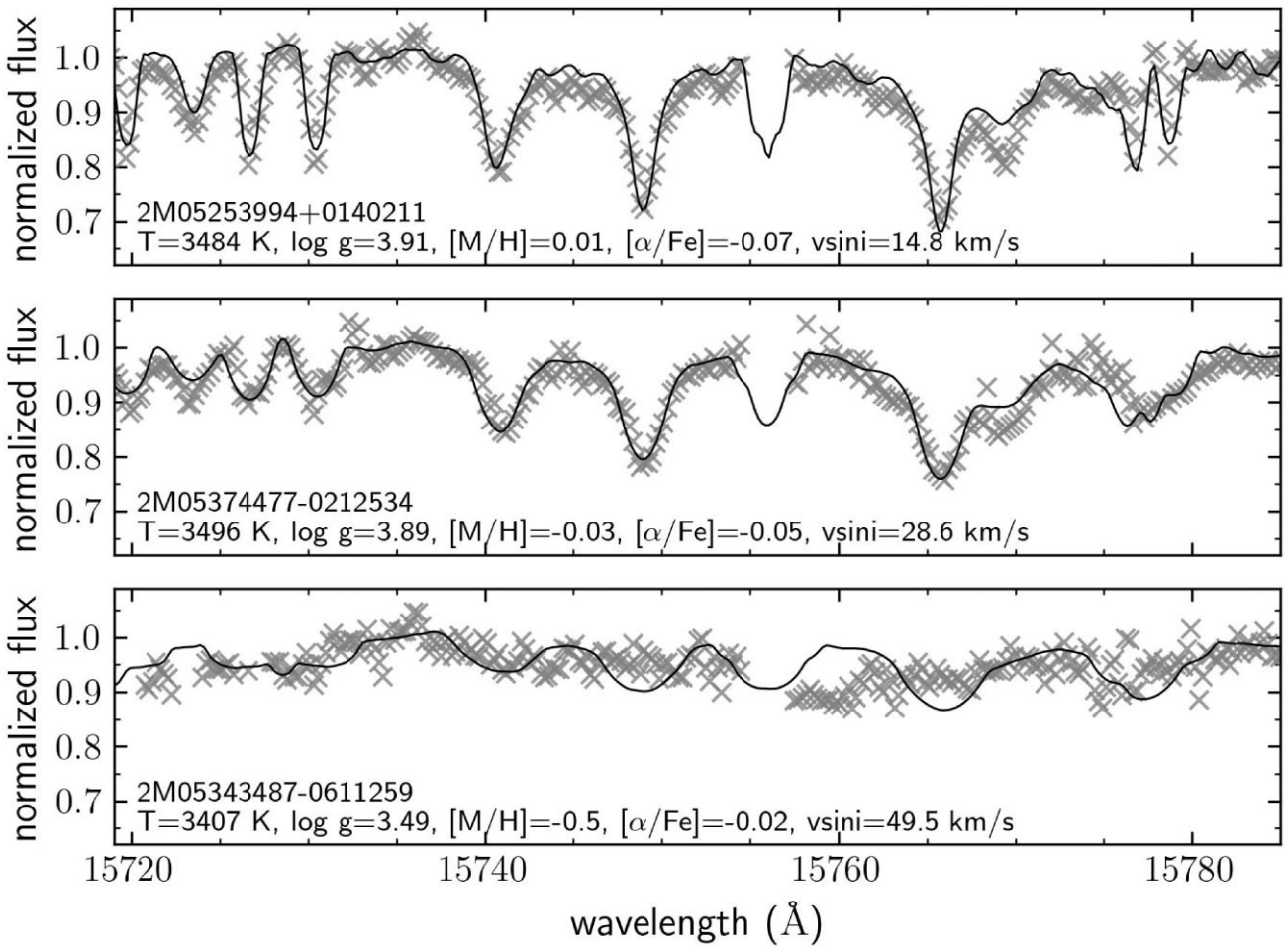


**Figure 3.** Small spectral window of three different observed spectra (grey crosses). In each panel, we overplot the synthetic spectra corresponding to the best-fitting atmospheric parameters derived with TONALLI. The upper and middle panels show good-quality fits, while in the bottom panel the fit quality deteriorates as TONALLI approaches the upper $v \sin i$ limit of the grid.

for main- and post-main sequence targets. In contrast, *Gaia* DR3 estimates are more uniformly distributed around ∼4.1 dex, yet they remain on average 0.20 dex higher than our determinations and, more importantly, higher than expected for the Orion age. Despite the observed trends, our best agreement is with ANet III, where our log $g$ values are on average 0.13 dex higher. The points in Fig. 5 are colour-coded by TONALLI $T_{\rm eff}$; however, no strong trend is observed. There is a slight indication that stars with higher log $g$ in ANet III and *Gaia* (middle and right panels) tend to be hotter in our analysis.

Finally, the [M/H] values exhibit a trend similar to that of log g, as shown in Fig. 6. We find the best agreement between our [M/H] values and the ASPCAP DR17 estimates, with our measurements being, on average, 0.02 ± 0.10 dex higher. In contrast, the [M/H] values from ANet III for Orion stars are more tightly constrained around solar metallicity (0.0 ± 0.2 dex), likely due to the spectral 'labels' used to train their neural network. Meanwhile, the *Gaia* DR3 metallicity estimates show substantial scatter across th e plot. This high dispersion is likely due to the low spectral resolution of the BP/RP spectra from which the [M/H] values were derived. Additionally, the *Gaia* metallicity estimates appear systematically too low for the types of sources studied here. Similarly to Fig. 5, we colour-coded the comparisons in Fig. 6 using TONALLI $T_{\rm eff}$. We found a mild trend in the ANet III panel, where lower [M/H] values appear to be associated with hotter stars in our analysis. This behaviour was previously reported for earlier versions of the ANet algorithm, which tended to predict lower metallicities for hotter stars (Olney et al. 2020). Although newer versions of the algorithm have improved in this regard, our results suggest that this issue may still persist to some extent in young stars.

The atmospheric parameters derived with TONALLI for the Orion stars span $T_{\rm eff}$ and log $g$ ranges consistent with expectations from evolutionary models. However, 22 sources exhibit metallicities below −0.50 dex, which may be incompatible with the young age of Orion and the chemical properties of the thin disc stellar population. Among these sources, nineteen (∼86 per cent) have projected rotational velocities ($v \sin i$) exceeding 47 km s$^{-1}$. In these cases, the actual stellar rotation may exceed the maximum $v \sin i$ value allowed in TONALLI (50 km s$^{-1}$). As we mentioned before, when this upper limit is reached, the algorithm struggles to reproduce the observed spectral line broadening. As a result, it compensates by artificially lowering the [M/H] in an attempt to match the shallow spectral features, leading to anomalously low values. As previously noted, the atmospheric parameters of sources with $v \sin i \geq 45$ km s$^{-1}$ should be considered with caution and treated as first-order approaches. For this reason, the low [M/H] values in these high $v \sin i$ stars are likely outliers rather than reliable measurements and should be discarded from further analysis.

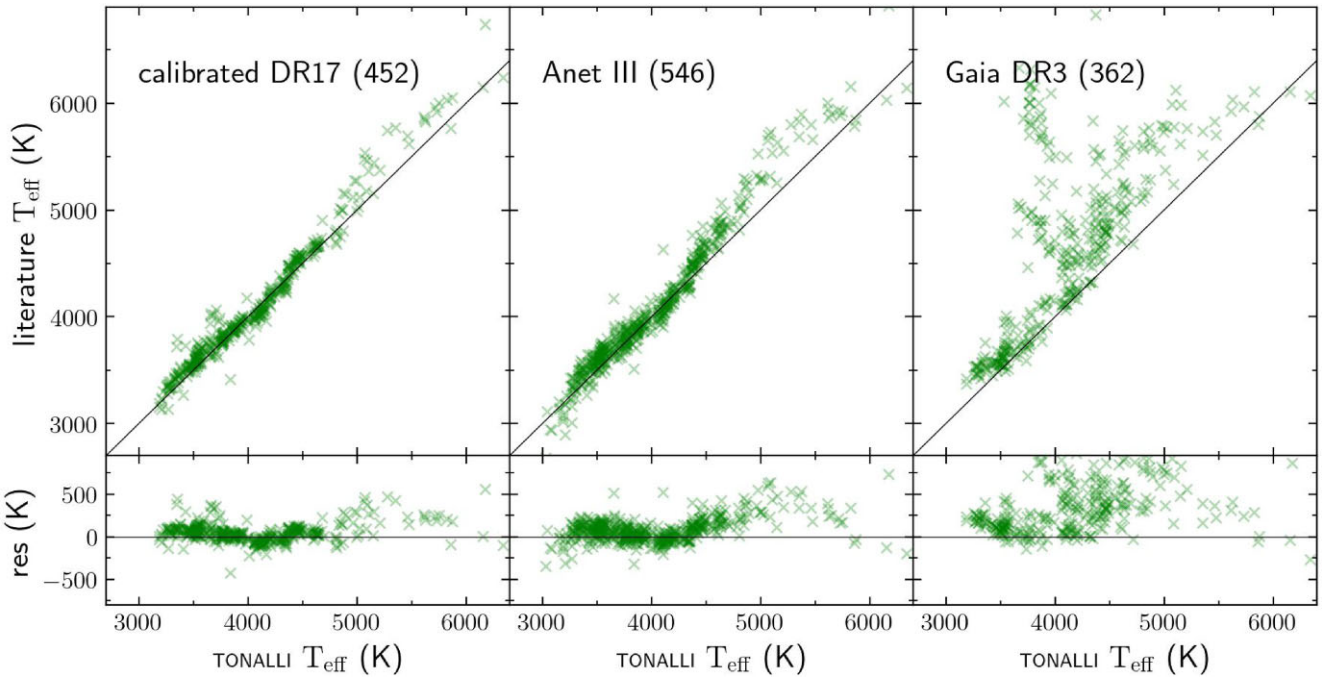


**Figure 4.** Comparison of the TONALLI $T_{eff}$ with the calibrated estimates of ASPCAP DR17 (Abdurro'uf et al. 2022), ANet III (Sizemore et al. 2024), and *Gaia* DR3 (Gaia Collaboration 2023). The number within the parenthesis is the stars included in each comparison. The lower panels are the differences between the literature and our estimates.

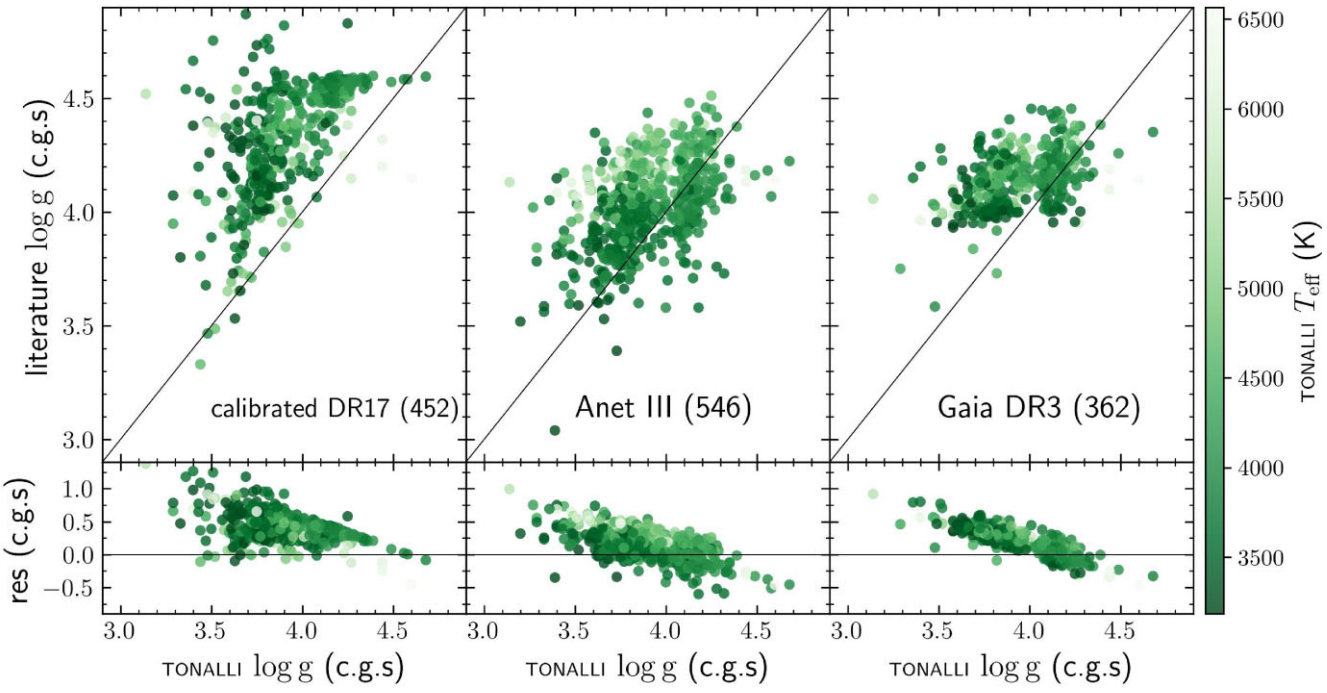


**Figure 5.** The same as Fig. 4 but for log $g$. The points are colour-coded by TONALLI $T_{eff}$.

## 4 CHEMICAL ABUNDANCE DETERMINATION

To determine the chemical abundances of our sample, we used the atmospheric parameters obtained from TONALLI, the Brussels automated code to characterize high-accuracy spectra (BACCHUS; Masseron, Merle & Hawkins 2016), and the reduced spectra of APOGEE DR17.

BACCHUS, computes on-the-fly synthetic spectra for a range of abundances that compares to observations on a line-by-line basis. The version of BACCHUS we used relies on the v15.1 of the 1D LTE radiative transfer code TURBOSPECTRUM (Plez 2012). To generate the synthetic spectra we employed a MARCS model atmosphere grid (Jönsson et al. 2020), the atomic line list of Smith et al. (2021),

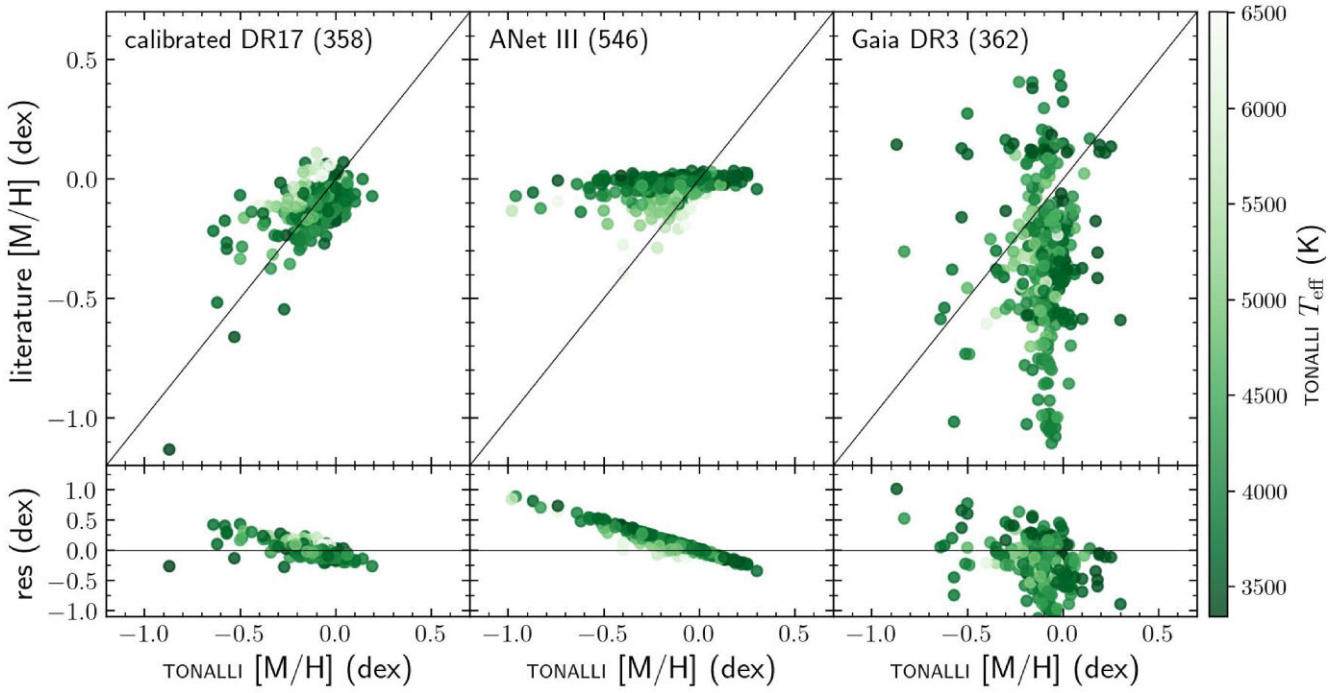


**Figure 6.** The same as Fig. 4 but for [M/H]. The points are colour-coded by TONALLI $T_{\rm eff}$.

and the molecular line lists for CO, CN, and OH of Li et al. (2015), Sneden et al. (2014) and Brooke et al. (2016), respectively.

Additionally, to compute a synthetic spectrum model, TURBOSPECTRUM needs to be provided with (or compute) the basic atmospheric parameters ($T_{\rm eff}$, log $g$, [M/H], [$\alpha$/Fe]), microturbulence velocity, a convolution parameter, which includes the instrumental and rotational broadening, and a standard solar composition, which in our case was that of Grevesse, Asplund & Sauval (2007). To derive chemical abundances, BACCHUS compared, within a 30 Å spectral window, the synthetic and observed spectra through four different methods, namely, *chi2*, *syn*, *eqw*, and *int* to find the best A(X)[4] abundance for each method. In this study, we used the *chi2* method, which minimizes the squared differences between observed and synthetic spectra. This method is the most balanced among the four.

For each star in our sample, we used the epoch-combined 1D APOGEE spectrum[5], the TONALLI $T_{\rm eff}$, log $g$, [M/H], and initially we used the line lists reported in López-Valdivia et al. (2024) and Grilo et al. (2024) that allowed us to access to twelve light elements: C, Na, Mg, Al, Si, K, Ca, Ti, V, Cr, Mn, and Fe.

We left the microturbulence velocity and the convolution parameter of BACCHUS to vary freely. However, we initialized the convolution parameter to be equal to $v \sin i$ value found in TONALLI, something of great importance, as with this, the convergence effectiveness of BACCHUS improved. The outcome of this process was the chemical abundance, together with a quality flag, SNR, and equivalent width for each atomic line in the line list as well as a value of microturbulence and convolution parameter for each star.

[4] $A(X) = \log(n_X/n_H) + 12$.

[5] We used the apStar spectra downloaded from the SDSS-IV science archive web app (SAW).

### 4.1 Final abundance and error

To compute the final abundances and their uncertainties, we used the best-fitting parameters derived with TONALLI. However, since these parameters have associated uncertainties, we adopted a Monte Carlo approach to propagate their effects on the abundance determinations. Specifically, for each star, we repeated the abundance determination procedure 100 times, each time perturbing the atmospheric parameters ($T_{\rm eff}$, log $g$, [M/H], and $v \sin i$) by randomly sampling values from a uniform distribution within their respective interquartile ranges as determined by TONALLI. In each iteration, we ran BACCHUS to compute the abundances for all available atomic lines, but selecting only lines with a good-fit flag and SNR greater than 100 to ensure high-quality measurements. As a result, for each star and each selected atomic line, we obtained a distribution of 100 abundance values. From this distribution, we adopted the median as the final abundance estimate and defined the uncertainty as the range between the minimum and maximum values found across the 100 iterations.

This procedure to obtain the uncertainties on the chemical abundances was time-consuming as BACCHUS is not parallelized. To solve this, we used the newly created GRID UNAM system, which allows us to run BACCHUS in a pseudo-parallel way to reduce the computing time by occupying as many threads available at a given time in a server grid distributed among various institutions. The Grid UNAM is a high-performance computing infrastructure that brings together various units within the National Autonomous University of Mexico (UNAM) to enable the efficient and collaborative use of computational and human resources. It operates through a 10 Gbps network that connects distributed computing and storage systems, offering both high-performance and high-throughput computing services. Its heterogeneous infrastructure includes powerful computing clusters and large-scale data storage supported by the MinIO[6] platform,

[6] https://min.io/

widely used for handling workloads in machine learning, data analytics, and scientific applications.

Recently, some studies have found trends between determined chemical abundances and the stellar parameters, mainly temperature (e.g. Kos et al. 2021; Grilo et al. 2024; Kos et al. 2025), derived from spectra of the same or similar spectral resolution. In Kos et al. (2025), there is an extended discussion on the trends they found between $T_{eff}$ and abundance value in stellar clusters. They argue that trends between abundance and another stellar parameter like gravity or $v \sin i$ might be the result of the relation of these parameters with $T_{eff}$, and that those trends disappear once detrending is applied to the abundances. Kos et al. (2025) observed two main behaviours in their analysis, thanks to the fact that they included a wide range of stars (e.g. giants and dwarfs) of different ages. They found a monotonic trend between 4800 and ∼6800 K, similar to the behaviour found by Grilo et al. (2024) in FGK dwarfs stars of the Pleiades. The second trend found by Kos et al. (2025) was for lower temperature stars, and it is steeper than the first, even showing a sharp upturn at ∼3800 K. Although the origin of the $T_{eff}$-abundance trends is not clear, there might be multifactorial causes related to physical processes (e.g. atomic diffusion) and processing issues (e.g. continuum fitting, linelists, atmospheric models) as suggested by Kos et al. (2025). Unveiling the nature of these trends is beyond the scope of this work; however, we favoured the interpretation that these trends are primarily driven by limitations in the atmospheric models and linelists. We refer the reader to section 4 of Kos et al. (2025) for a more detailed discussion on the origin of these trends. As a practical solution, we identified and excluded from our analysis those atomic lines that exhibit a significant systematic trend as a function of either $T_{eff}$ or log $g$.

We computed the Spearman correlation coefficient ($r$) to discard those lines that exhibited a moderate to high linear correlation between abundance and $T_{eff}$ and abundance and log $g$. To reinforce the significance of the $r$ coefficient computed, we randomly varied the abundance value within its error and recomputed Pearson coefficients. After 300 iterations, we computed a mean $r$ value and the standard deviation to assess the correlation of the examined atomic line with $T_{eff}$ and log $g$. We then selected lines with a weak linear correlation, corresponding to $r \pm \sigma_r$ values within the ±0.35 range. In Fig. 7, as an example, we present the abundance values derived with BACCHUS for three different carbon lines, plotted as a function of $T_{eff}$ (left column) and log $g$ (right column). Among the three lines, only the one identified as C3 (top panels), located at approximately 15 784 Å, was included in our final analysis, as it exhibits $r$ below 0.35 with both $T_{eff}$ and log $g$. In contrast, the C4 and C5 lines failed to meet this criterion, with only one of their coefficients falling below the threshold, and were therefore excluded from further analysis. We found 19 atomic lines of 6 elements (C, Mg, Si, K, Ti, and Fe) that met our $r$ value requirement, and those that we included in our subsequent analysis. In Table 3, we present the basic information of the atomic lines used in this work. It is important to mention that the selection threshold of the $r$ coefficients is set arbitrarily, and if we relaxed it, more lines would meet the criteria; however, abundance trends might appear in our results.

The exclusion of tendentious lines enhances the robustness of our abundance determinations, reducing the likelihood that observed variations arise from the line list itself. This approach enables more reliable comparisons across different groups or stellar members, minimizing spurious trends with effective temperature or surface gravity. While all abundance analyses inherently depend on the adopted model atmospheres and line lists, our methodology is designed to mitigate such dependencies. Additionally, although some

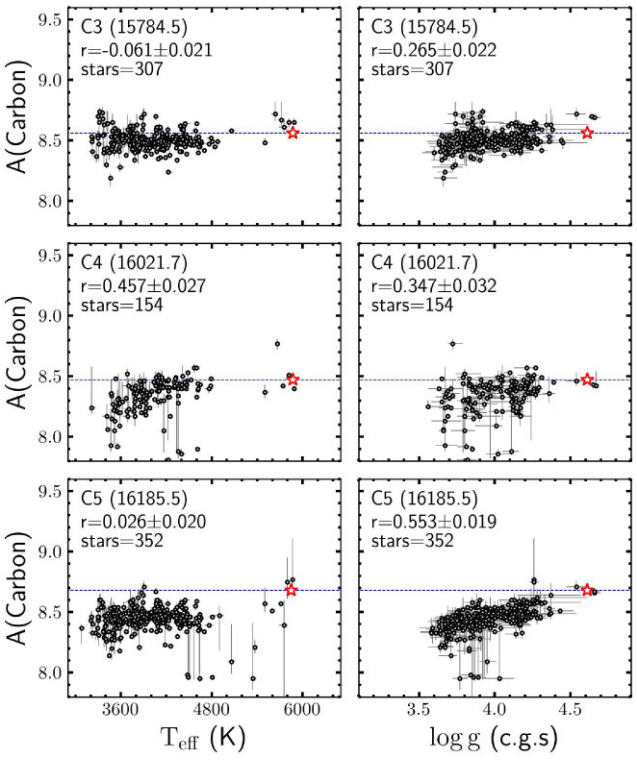


**Figure 7.** Logarithmic abundance values found with BACCHUS for three different carbon lines (C3, C4, C5) are shown as a function of $T_{eff}$ (left) and log $g$ (right). The number in parentheses indicates the wavelength of each line, while $r$ represents the mean Spearman correlation coefficient calculated for the corresponding data set. The red star and dashed line indicate the solar abundance associated with the line under analysis. Based on our selection criteria (see the text), only the line identified as C3 was ultimately included in our analysis.

**Table 3.** Basic information of the 19 atomic lines used in this study. The last column is the solar abundance determined using the APOGEE DR17 Vesta asteroid spectrum.

| λ (Å) | Element | χ (eV) | log gf | Van der Wals | $A(X)_{Vesta}$ |
|---|---|---|---|---|---|
| 15784.536 | C | 9.631 | −0.588 | −6.99 | 8.56 ± 0.02 |
| 15740.716 | Mg | 5.931 | −0.323 | −6.84 | 7.51 ± 0.06 |
| 15879.521 | Mg | 5.946 | −2.102 | −6.91 | 7.66 ± 0.02 |
| 15884.454 | Si | 5.954 | −0.945 | −7.11 | 7.64 ± 0.02 |
| 16060.009 | Si | 5.954 | −0.452 | −7.07 | 7.42 ± 0.02 |
| 16094.787 | Si | 5.964 | −0.088 | −7.10 | 7.51 ± 0.05 |
| 16215.670 | Si | 5.954 | −0.565 | −7.21 | 7.46 ± 0.02 |
| 16241.833 | Si | 5.964 | −0.762 | −7.13 | 7.50 ± 0.02 |
| 16828.159 | Si | 5.984 | −1.058 | −7.10 | 7.62 ± 0.04 |
| 15163.067 | K | 2.670 | 0.632 | −6.82 | 4.93 ± 0.02 |
| 15168.377 | K | 2.670 | 0.441 | −6.82 | 5.06 ± 0.02 |
| 16635.158 | Ti | 2.345 | −1.771 | −7.49 | 5.05 ± 0.05 |
| 15207.526 | Fe | 5.385 | 0.067 | −7.21 | 7.65 ± 0.03 |
| 15244.974 | Fe | 5.587 | −0.134 | −7.01 | 7.49 ± 0.03 |
| 15723.586 | Fe | 5.621 | −0.011 | −7.05 | 7.51 ± 0.03 |
| 15904.324 | Fe | 6.365 | −0.154 | −7.19 | 7.43 ± 0.02 |
| 15920.642 | Fe | 6.258 | −0.011 | −7.01 | 7.45 ± 0.02 |
| 16125.899 | Fe | 6.351 | 0.618 | −6.91 | 7.54 ± 0.03 |
| 16316.320 | Fe | 6.280 | 0.857 | −6.90 | 7.49 ± 0.03 |

elements can exhibit departures from LTE that introduce trends with $T_{\rm eff}$ and log $g$, these effects are expected to be smaller in the near-infrared, particularly for cool dwarf stars with near-solar metallicity, than at optical wavelengths (e.g. Osorio et al. 2020; Olander, Heiter & Kochukhov 2021). To quantify this, we used the publicly available MPIA non-LTE corrections service (https://gemini-web.mpia.de/), which compiles results from infrared studies of Mg, Si, Ti, and Fe (e.g. Bergemann et al. 2012, 2013, 2015). For these elements, the corrections are negligible (typically <0.02 dex). For potassium, the corrections are below 0.1 dex (Osorio et al. 2020), which is comparable to the mean uncertainty in our K abundance (0.06 dex)

#### 4.1.1 [X/H] abundance ratios

We computed [X/H][7] ratio for each selected line using the solar abundance obtained, in the same fashion as our sample, from the APOGEE DR17 Vesta spectrum (Table 3). We used the 1D solar atmospheric parameters reported by Adame et al. (2024). If we had more than one selected line from the same element, we computed the mean value and propagated the individual errors to obtain a final uncertainty.

We did not measure the abundances for all the stars of our sample for three main reasons: (i) the temperature of the star (too hot or cold) interfered to measure reliably some of the selected atomic lines; (ii) there were cases where some spectral regions presenting data reduction issues, and (iii) the $v \sin i$ of the star was high (>30 km s$^{-1}$), implying a higher degree of line blending. We also did not report [X/H] abundance estimations higher than 0.5 dex and lower than −0.75 dex, as we considered them as values incompatible with the stellar population we are working with. We measured the abundance of two or more elements for 340 stars (∼62 per cent) of our sample, that we report along with their respective errors in Table 2. Additionally, we examined the relationship between the microturbulence values derived with BACCHUS and the mean elemental abundances. No strong correlations were found, with Pearson coefficients ranging from $r = -0.29$ to $-0.07$ across all elements analysed. We also investigated the potential correlation between $v \sin i$ and the BACCHUS microturbulence values, again finding no significant trend. The median BACCHUS microturbulence in our sample is 1.1 km s$^{-1}$, and individual values for each star are reported in Table 2.

## 5 CHEMICAL ABUNDANCES OF ORION

According to our [X/H] abundance ratios, the whole Orion complex presented subsolar abundances for all six elements studied. This result aligns with the presence of a negative vertical metallicity gradient observed in the solar neighbourhood using samples of giant and hot stars (e.g. Hawkins 2023; Hackshaw et al. 2024). The Orion star-forming region, located approximately 100–180 pc below the Galactic mid-plane (e.g. Zucker et al. 2020; Großschedl et al. 2021), lies along the Radcliffe Wave (Alves et al. 2020), where similar trends have been reported. Furthermore, our findings agree with Galactic disc metallicity maps, which show average metallicities of about –0.10 to –0.05 dex at the position of our sample (e.g. Poggio et al. 2022; Martinez-Medina, Poggio & Moreno-Hilario 2025). While most of the aforementioned studies focus on evolved or massive stars, the agreement with our results based on young, cool stars is promising. It suggests that this type of analysis could be extended to other star-forming regions to further investigate the radial and vertical metallicity gradients in the Galactic disc.

Fig. 8 shows box plots of our [X/H] values to visually analyse the abundance ratios in the different Orion groups. As previously mentioned, the median abundance ratios for all elements are subsolar. Despite this, most of them show a dispersion that still makes these ratios consistent with solar abundances.

In terms of comparing the different groups, although there might be some differences between median abundance values, this was not significant, and all of them were consistent within their corresponding MAD, suggesting that the Orion complex was chemically homogeneous in all six elements analysed here (see Table 4). Our results agreed with Kos et al. (2021), where they also found slightly subsolar abundances for Orion members and chemical homogeneity.

Comparing chemical abundances across different studies presents inherent challenges, as methodologies, atmospheric models, and standard solar scales often differ. In many cases, a calibration to a common framework is necessary to ensure meaningful comparisons (e.g. Hinkel et al. 2014). None the less, relative comparisons can still provide valuable insight.

To place the Orion members in context, we used the sample from López-Valdivia et al. (2024) as a reference for the chemical abundances of the solar neighbourhood. This comparison sample includes G-, K-, and M-type stars with effective temperatures between 3300 and 6000 K, all located within 100 pc of the Sun. We adopted the atmospheric parameters reported in that study and applied the same abundance determination methodology used in this work to ensure consistency between the two data sets.

The nearby sample is highly diverse, comprising stars with a wide range of masses and ages. To ensure a homogeneous comparison between Orion and the solar neighbourhood, we divided both samples into two $T_{\rm eff}$ bins: stars with $T_{\rm eff} \leq 4000$ K (M-type stars), and stars with temperatures between 4000 and 5000 K (K-type stars). We also restricted the comparison to stars with [Fe/H] values within ±0.5 dex. These two temperature bins encompass 93 per cent of the Orion stars for which BACCHUS chemical abundances were determined.

We compared the Orion [X/H] abundances to those of the solar neighbourhood and found that the median values are quite similar between both samples in both $T_{\rm eff}$ bins (see Table 5). This agrees with previous studies that report remarkable chemical homogeneity across the solar neighbourhood, based on both nebular and stellar tracers (Esteban et al. 2022; Méndez-Delgado et al. 2022; Ritchey et al. 2023).

However, Kolmogorov–Smirnov (KS) tests indicate that the two populations are statistically different, with very low $\mathcal{P}$(KS) values. Since the nearby sample contains many more stars than the Orion sample, we tested whether this difference in sample size might be responsible for the low KS probabilities. We performed a bootstrap procedure, randomly drawing subsamples from the nearby population with the same number of stars as the Orion sample, and computed the KS test 10 000 times. We report the median of the resulting $\mathcal{P}$(KS) distribution in Table 5. The low median $\mathcal{P}$(KS) values persisted, reinforcing our initial result.

Since both samples were restricted in $T_{\rm eff}$ and [Fe/H], the observed differences might be, at least partially, attributed to differences in log $g$, which can be interpreted as a proxy for age. For M-type stars, we found median log $g$ values (and MAD) of 3.86 ± 0.17 for Orion and 4.78 ± 0.05 for the main-sequence stars. This difference is smaller for K-type stars, where the medians were 4.06 ± 0.13 and 4.68 ± 0.04, respectively.

[7]The [X/H] = A(X)$_{\rm star}$ − A(X)$_{\odot}$, where the A(X) are the BACCHUS abundances found.

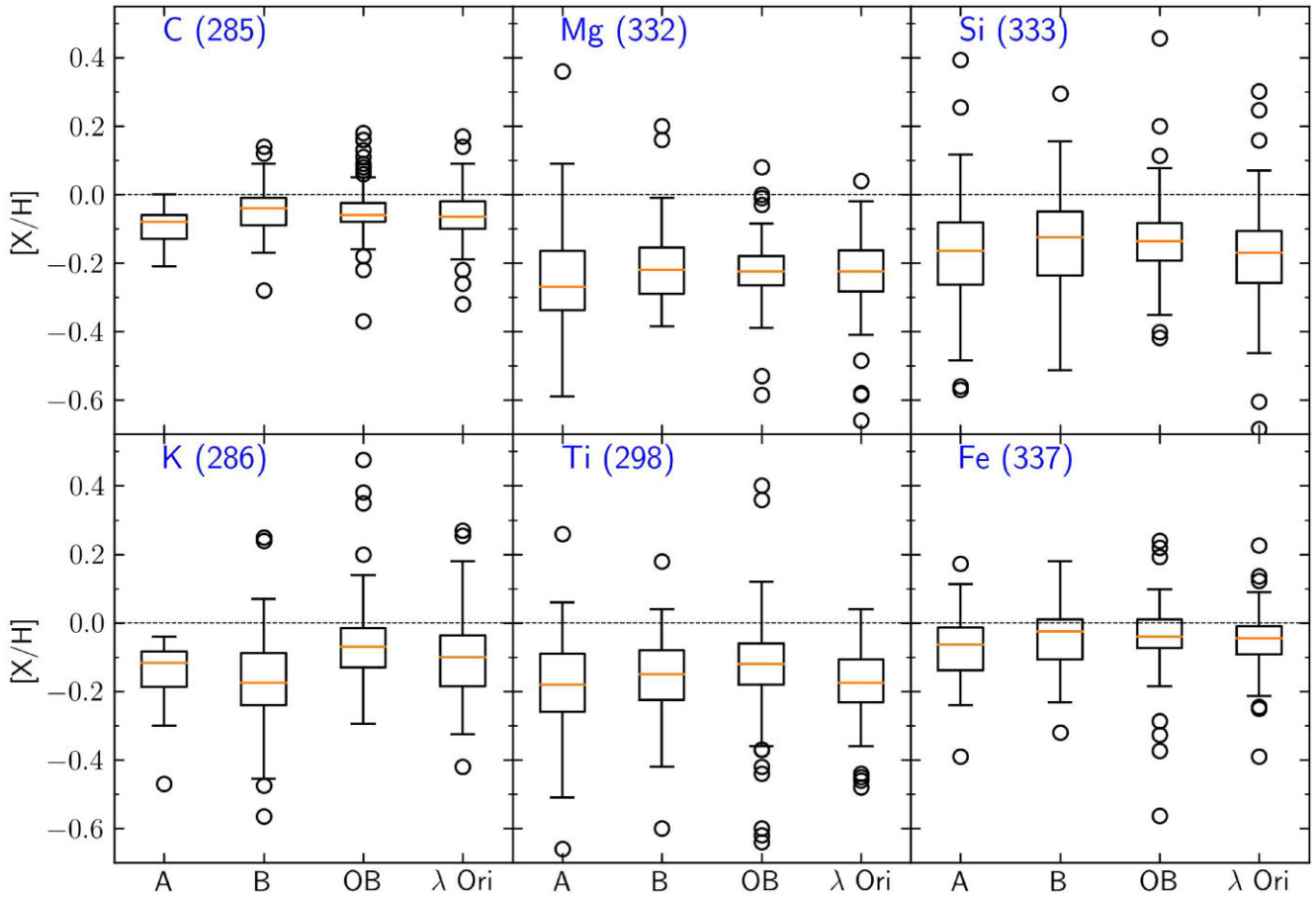


**Figure 8.** Boxplot of the [X/H] abundance ratios derived in this work for each Orion group. The box encloses data between the inter-quartile range (IQR) while the whiskers extend from the box to 1.5×IQR. The orange horizontal line is the median value. The total number of stars for each element is within parentheses. Our determinations suggest that Orion is chemically homogeneous, as supported by the low MAD shown in Table 4.

**Table 4.** Median abundance values for each [X/H] and for each Orion group. We present the number of stars included in the computation,#, followed by the median and median absolute deviation of our [X/H] estimations.

| Group | [C/H] | | [Mg/H] | | [Si/H] | | [K/H] | | [Ti/H] | | [Fe/H] | |
|---|---|---|---|---|---|---|---|---|---|---|---|---|
| | # | $\tilde{x}\pm$MAD | # | $\tilde{x}\pm$MAD | # | $\tilde{x}\pm$MAD | # | $\tilde{x}\pm$MAD | # | $\tilde{x}\pm$MAD | # | $\tilde{x}\pm$MAD |
| λ Ori | 74 | $-0.07 \pm 0.04$ | 78 | $-0.23 \pm 0.06$ | 77 | $-0.17 \pm 0.07$ | 71 | $-0.10 \pm 0.07$ | 76 | $-0.17 \pm 0.07$ | 79 | $-0.05 \pm 0.04$ |
| Orion A | 29 | $-0.08 \pm 0.03$ | 51 | $-0.27 \pm 0.08$ | 52 | $-0.16 \pm 0.09$ | 32 | $-0.12 \pm 0.04$ | 37 | $-0.18 \pm 0.09$ | 52 | $-0.06 \pm 0.06$ |
| Orion B | 43 | $-0.04 \pm 0.04$ | 51 | $-0.22 \pm 0.07$ | 50 | $-0.12 \pm 0.09$ | 44 | $-0.17 \pm 0.07$ | 47 | $-0.15 \pm 0.07$ | 51 | $-0.03 \pm 0.06$ |
| Orion OB | 139 | $-0.06 \pm 0.03$ | 152 | $-0.23 \pm 0.04$ | 154 | $-0.14 \pm 0.05$ | 139 | $-0.07 \pm 0.06$ | 138 | $-0.12 \pm 0.06$ | 155 | $-0.04 \pm 0.04$ |

**Table 5.** Median [X/H] values and MADs for Orion young stars and the main-sequence sample from López-Valdivia et al. (2024), calculated in two different $T_{\rm eff}$ bins. Columns 4 and 7 show the median KS test *p*-values obtained through a bootstrapping procedure comparing both populations. Only stars in the range $-0.5 \leq$ [Fe/H] $\leq +0.5$ were included in the comparisons.

| | $T_{\rm eff} \leq 4000$ | | | $4000 < T_{\rm eff} \leq 5000$ | | |
|---|---|---|---|---|---|---|
| [X/H] | Orion stars | Main-sequence stars | $\mathcal{P}$(KS) | Orion stars | Main-sequence stars | $\mathcal{P}$(KS) |
| C | $-0.05 \pm 0.04$ (148) | $-0.17 \pm 0.11$ (327) | 2.4e−15 | $-0.07 \pm 0.02$ (128) | $-0.04 \pm 0.09$ (337) | 3.3e−06 |
| Mg | $-0.22 \pm 0.06$ (183) | $-0.26 \pm 0.09$ (441) | 1.6e−03 | $-0.24 \pm 0.04$ (137) | $-0.15 \pm 0.09$ (401) | 3.5e−12 |
| Si | $-0.18 \pm 0.08$ (183) | $-0.22 \pm 0.11$ (449) | 7.3e−03 | $-0.12 \pm 0.04$ (138) | $-0.10 \pm 0.09$ (411) | 1.5e−05 |
| K | $-0.13 \pm 0.08$ (149) | $-0.02 \pm 0.08$ (348) | 2.1e−09 | $-0.08 \pm 0.04$ (128) | $-0.06 \pm 0.08$ (404) | 1.0e−03 |
| Ti | $-0.16 \pm 0.08$ (163) | $-0.23 \pm 0.10$ (418) | 1.2e−05 | $-0.13 \pm 0.07$ (127) | $-0.05 \pm 0.10$ (400) | 1.5e−06 |
| Fe | $-0.04 \pm 0.05$ (188) | $-0.18 \pm 0.13$ (647) | 1.1e−17 | $-0.04 \pm 0.04$ (139) | $-0.05 \pm 0.10$ (411) | 1.6e−04 |

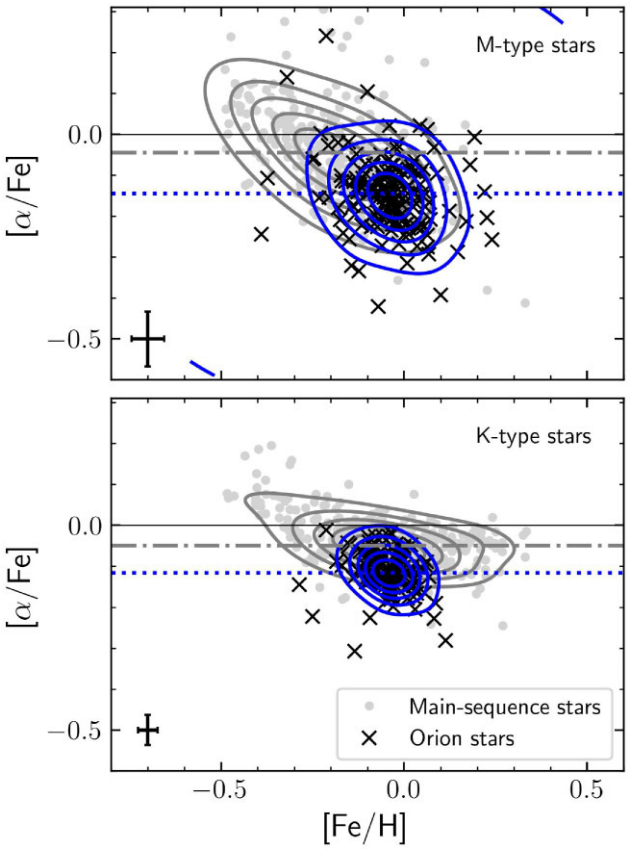


**Figure 9.** Tinsley–Wallerstein diagram for the Orion members (black crosses) and the main-sequence stars (grey points) of López-Valdivia et al. (2024) using the abundances determined in this study for M-type stars (upper panel) and K-type stars (bottom panel). The [$\alpha$/Fe] ratio corresponds to the weighted average of our [Mg/Fe], [Si/Fe], and [Ti/Fe]. The dotted and dash–dotted lines represent the median value of [$\alpha$/Fe] for the Orion and main-sequence stars, respectively. We also included number density contours for Orion (blue) and the main-sequence stars (grey). Error bars in the lower-left corner of each panel represent the median uncertainties in the [Fe/H] and [$\alpha$/Fe] for Orion stars.

Additionally, using our Mg, Si, and Ti abundance determinations, we computed [$\alpha$/Fe] for both samples. We define [$\alpha$/Fe] as a weighted average of the [Mg/Fe], [Si/Fe], and [Ti/Fe] abundance ratios. In this calculation, more weight is given to the measurements with smaller uncertainties, so that the most precise values contribute more significantly to the final [$\alpha$/Fe] estimate. The resulting [$\alpha$/Fe] values and their corresponding uncertainties, calculated as the error in the weighted mean, are listed in Table 2.

For the M-type stars, the median [$\alpha$/Fe] were $-0.14 \pm 0.05$ and $-0.04 \pm 0.06$ for Orion and the main-sequence samples, respectively. Similar values were found for the K-type stars: $\mathbf{-0.12 \pm 0.03}$ for Orion and $\mathbf{-0.05 \pm 0.03}$ for the main-sequence stars.

Fig. 9 shows the [Fe/H]–[$\alpha$/Fe] (Tinsley–Wallerstein) diagram for both populations. The abundances of the main-sequence stars fall within the expected locus of thin disc stars (e.g. Neves et al. 2009). The Orion members, on the other hand, occupy a more constrained region in this diagram and appear to be shifted toward lower [$\alpha$/Fe] and subsolar [Fe/H] values. This may suggest that the interstellar medium from which these younger stars formed has already been enriched by the stellar evolution of older stellar generations. From the evolutionary perspective, the chemical abundance of the interstellar medium (ISM) is a better comparison to the abundance of young stars, as the difference in the evolutionary stage is smaller than with the main-sequence stars. Moreover, the main-sequence stars of López-Valdivia et al. (2024) are located at different distances and positions in the Galaxy, something that might also introduce uncertainties.

Méndez-Delgado et al. (2022) analysed the radial abundance gradients of He, C, N, O, Ne, S, Cl, and Ar in the Galaxy using optical spectra of 42 H II regions, including M42 (the Orion Nebula). They determined a carbon abundance of M42 of $8.34 \pm 0.02$, which translates to $-0.05 \pm 0.05$, $-0.12 \pm 0.04$, and $-0.17 \pm 0.09$ if the standard solar composition of Grevesse et al. (2007), Asplund, Amarsi & Grevesse (2021), or Lodders, Bergemann & Palme (2025) is adopted. The median [C/H] we have determined for the whole Orion complex is $-0.06 \pm 0.03$, which agrees, when we take into account the errors, with the three different values of M42.

It is important to note that the C/H determination by Méndez-Delgado et al. (2022) in the Orion Nebula is based on the C II $\lambda$4267 recombination line (RL), whose ratio with H $\beta$ is virtually insensitive to the physical conditions of the gas. In contrast, the collisionally excited lines (CELs) C III] $\lambda\lambda$1907, 1909, measured in the UV by Walter, Dufour & Hester (1992), are highly sensitive to the electron temperature ($T_e$) of the gas, and yield a C/H abundance approximately ~0.4 dex lower (Esteban et al. 2004). The CEL-nebular calculations are in tension with the stellar abundances reported in this work.

The long-standing discrepancy between abundances derived from CELs and RLs has been widely debated in the literature (Chen et al. 2023; Méndez-Delgado et al. 2023, 2024a). Determining which of these two methods yields more accurate chemical abundances is critical to our understanding of the formation and chemical evolution of galaxies (Curti 2025). The stellar abundance measurements carried out by our group may offer crucial insight into this issue, providing an independent tracer of the true chemical content. The good agreement between RL-based carbon abundances and those derived from stellar objects supports the view that RLs may provide more reliable abundance estimates (Méndez-Delgado et al. 2023), possibly indicating that internal temperature fluctuations within the ionized gas (Peimbert 1967), or other physical processes, may systematically bias CEL-based nebular abundances downward.

The Orion nebula, or M42, is spatially located around the Orion A group; thus, the stars of this group are a better test bed to sense the composition differences between the young stars and the H II region. In Fig. 8 (and Table 4), there is a hint that members of the Orion A group possess a slightly lower carbon abundance than stars in the other three groups, aligning with the subsolar abundances reported by Méndez-Delgado et al. (2022) for M42. The median [C/H] abundance for Orion A is $-0.08 \pm 0.03$, the lowest in absolute value, although not significant if errors are considered, among all the Orion groups. This comparison represents a valuable starting point for future studies combining the APOGEE-2 data with the SDSS-V Local Volume Mapper, which will provide more and better Galactic ISM spectra. As we showed, the combination of both surveys gives us the possibility to do direct comparisons of the composition of gas and young stars for a specific region, such as in the case of Orion, and helps us to constrain Galactic chemical evolution models. Additionally, we can investigate gradients within star-forming regions as well as within the Galaxy through the characterization of young stars (Hernández-Aburto et al., in preparation), and connect this with the previous determinations made through the composition of the interstellar medium.

The analysis of multiple chemical elements in stellar parameters is a rapidly growing area of research, not only within the stellar community but also in the context of nebular studies. As demonstrated by Méndez-Delgado et al. (2024b), comparing stellar Fe-

based metallicities with nebular O-based metallicities, as has been done by some authors using low-resolution spectra (Bresolin et al. 2016), is not only insufficient, but may also introduce systematic biases in the interpretation of chemical abundances, particularly in the broader context of Galaxy evolution.

## 6 SUMMARY AND REMARK CONCLUSIONS

We determined atmospheric parameters ($T_{eff}$, log $g$, [M/H], [$\alpha$/Fe], and $v \sin i$) for a sample of 548 young stars in the Orion complex, using the spectral analysis code TONALLI (Adame et al. 2024). These stars, located in four subgroups (A, B, OB, and $\lambda$ Ori), were selected based on the absence of infrared excess, identified via their position in the $J$–($K - W3$) colour–magnitude diagram. This selection minimizes the impact of continuum veiling on our parameter estimates. The atmospheric parameters derived with TONALLI, particularly $T_{eff}$ and log $g$, are consistent with evolutionary models for stars at the age of Orion.

Using these parameters, we then applied the BACCHUS code (Masseron et al. 2016) to determine the chemical abundances of C, Mg, Si, K, Ti, and Fe. We obtained reliable abundances for at least two elements in 340 stars with projected rotational velocities $v \sin i < 30$ km s$^{-1}$, where line blending does not severely affect the spectra. In addition, we analysed the spectrum of Vesta to determine the solar reference abundances used in this study.

The Orion stars exhibit subsolar [X/H] abundance ratios, in agreement with previous findings (Kos et al. 2021). We also find chemical homogeneity across the subgroups Orion A, B, $\lambda$ Ori, and Orion OB in all six elements analysed. To provide context for the Orion abundances, we determined chemical abundances for a nearby sample of main-sequence stars, representing the solar neighbourhood. While the median [X/H] values in Orion are broadly consistent with those in the solar neighbourhood, a Kolmogorov–Smirnov (KS) test indicates that the two populations are statistically distinct.

Among the elements studied, three are $\alpha$-elements (Mg, Si, Ti), allowing us to compute [$\alpha$/Fe] ratios for both the young Orion stars and the nearby main-sequence sample. We find that Orion members have systematically lower median [$\alpha$/Fe] values compared to solar neighbourhood stars, which may reflect the chemical evolution of the Galaxy.

Finally, we compared the median carbon abundance in Orion A with measurements from the Orion Nebula (M42) based on RLs (Méndez-Delgado et al. 2022). We find good agreement when the logarithmic abundance in M42 is referenced to the solar value from Lodders (2003).

The atmospheric parameters and chemical abundances presented here represent a first step toward a homogeneous chemical characterization of young stars. Future work should aim to include stars with low to moderate infrared excesses, as well as to explore chemical abundances in fast rotators. This may be achieved through spectral deblending techniques and/or higher spectral resolution. These populations – stars with infrared excess and high rotation rates – represent a substantial fraction of the young stellar population in Orion and are essential for achieving a comprehensive understanding of the region's chemical evolution.

## ACKNOWLEDGEMENTS

We thank the referee for their helpful comments. RL-V and LA acknowledge support from Secretaría de Ciencia, Humanidades, Tecnología e Inovacción (SECIHTI) through a postdoctoral fellowship within the program 'Estancias posdoctorales por México'. SV gratefully acknowledges the support provided by Fondecyt Regular n. 1220264 and by the ANID BASAL project FB210003. JEM-D acknowledges financial support from the UNAM/DGAPA/PAPIIT/IG101025 and UNAM/DGAPA/PAPIIT/IG104325 grants. CR-Z, RL-V, JH, LA, and JS acknowledge financial support from UNAM/DGAPA/PAPIIT/IG101723 and SECIHTI nd project CONAHCYT Ciencia Frontera 86372 (entitled Citlalcoatl). Funding for the SDSS-IV has been provided by the Alfred P. Sloan Foundation, the U.S. Department of Energy Office of Science, and the Participating Institutions. SDSS-IV acknowledges support and resources from the Center for High-Performance Computing at the University of Utah. The SDSS website is www.sdss.org. SDSS-IV is managed by the Astrophysical Research Consortium for the Participating Institutions of the SDSS Collaboration including the Brazilian Participation Group, the Carnegie Institution for Science, Carnegie Mellon University, the Chilean Participation Group, the French Participation Group, Harvard-Smithsonian Center for Astrophysics, Instituto de Astrofísica de Canarias, The Johns Hopkins University, Kavli Institute for the Physics and Mathematics of the Universe (IPMU)/University of Tokyo, Lawrence Berkeley National Laboratory, Leibniz Institut für Astrophysik Potsdam (AIP), Max-Planck-Institut für Astronomie (MPIA Heidelberg), Max-Planck-Institut für Astrophysik (MPA Garching), Max-Planck-Institut für Extraterrestrische Physik (MPE), National Astronomical Observatories of China, New Mexico State University, New York University, University of Notre Dame, Observatário Nacional/MCTI, The Ohio State University, Pennsylvania State University, Shanghai Astronomical Observatory, United Kingdom Participation Group, Universidad Nacional Autónoma de México, University of Arizona, University of Colorado Boulder, University of Oxford, University of Portsmouth, University of Utah, University of Virginia, University of Washington, University of Wisconsin, Vanderbilt University, and Yale University. This research has made use of the SIMBAD database, operated at CDS, Strasbourg, France. This work made use of the high-throughput computing (HTC) infrastructure and the optimization of computing resources of the project Grid UNAM (https://grid.unam.mx/) at the Universidad Nacional Autónoma de México. Participating Institutions of the project Grid UNAM includes Dirección General de Cómputo y de Tecnologías de Información y Comunicación (DGTIC), Laboratorio de Modelos y Datos Científicos (LAMOD), Instituto de Ciencias de la Atmósfera y Cambio Climático (ICAyCC), Instituto de Astronomía (IA) and Instituto de Ciencias Nucleares (ICN). We also thank the members of technical and development staff of the project Grid UNAM for their continuous support.

## DATA AVAILABILITY

Table 2 is available in the online supplementary material of the paper and at CDS via anonymous ftp to cdsarc.u-strasbg.fr (130.79.128.5) or via https://cdsarc.cds.unistra.fr/viz-bin/cat/J/MNRAS/Vol/num.

## REFERENCES

Abdurro'uf et al., 2022, ApJS, 259, 35
Adame L., Román-Zúñiga C., Hernández J., López-Valdivia R., Sánchez E., 2024, RAS RAS Tech. Instr. Instruments, 3, 771
Almeida A. et al., 2023, ApJS, 267, 44
Alves J. et al., 2020, Nature, 578, 237
Asplund M., Amarsi A. M., Grevesse N., 2021, A&A, 653, A141

Bergemann M., Kudritzki R.-P., Plez B., Davies B., Lind K., Gazak Z., 2012, ApJ, 751, 156
Bergemann M., Kudritzki R.-P., Würl M., Plez B., Davies B., Gazak Z., 2013, ApJ, 764, 115
Bergemann M., Kudritzki R.-P., Gazak Z., Davies B., Plez B., 2015, ApJ, 804, 113
Biazzo K., Randich S., Palla F., Briceño C., 2011, A&A, 530, A19
Biazzo K., Alcalá J. M., Covino E., Sterzik M. F., Guillout P., Chavarría-K. C., Frasca A., Raddi R., 2012, A&A, 542, A115
Blaauw A., 1964, ARA&A, 2, 213
Blanton M. R. et al., 2017, AJ, 154, 28
Bresolin F., Kudritzki R.-P., Urbaneja M. A., Gieren W., Ho I. T., Pietrzyński G., 2016, ApJ, 830, 64
Brooke J. S. A., Bernath P. F., Western C. M., Sneden C., Afşar M., Li G., Gordon I. E., 2016, J. Quant. Spec. Radiat. Transf., 168, 142
Brown A. G. A., Hartmann D., Burton W. B., 1995, A&A, 300, 903
Cantó J., Curiel S., Martínez-Gómez E., 2009, A&A, 501, 1259
Chen Y., Bressan A., Girardi L., Marigo P., Kong X., Lanza A., 2015, MNRAS, 452, 1068
Chen Y. et al., 2023, Nat. Astron., 7, 771
Cottaar M. et al., 2014, ApJ, 794, 125
Cottaar M. et al., 2015, ApJ, 807, 27
Cui X.-Q. et al., 2012, Res. Astron. Astrophys., 12, 1197
Cunha K., Lambert D. L., 1994, ApJ, 426, 170
Cunha K., Smith V. V., Lambert D. L., 1998, ApJ, 493, 195
Curti M., 2025, preprint (arXiv:2504.08933)
Cutri R. M. et al., 2003, The IRSA 2MASS All-Sky Point Source Catalog, NASA/IPAC Infrared Science Archive. 2MASS All Sky Catalog of Point Sources. Available at: http://irsa.ipac.caltech.edu/applications/Gator/
Cutri R. M. et al., 2013, Explanatory Supplement to the AllWISE Data Release Products. Available at: http://wise2.ipac.caltech.edu/docs/release/allwise/expsup
D'Orazi V., Randich S., Flaccomio E., Palla F., Sacco G. G., Pallavicini R., 2009, A&A, 501, 973
Da Rio N. et al., 2016, ApJ, 818, 59
Da Rio N. et al., 2017, ApJ, 845, 105
De Silva G. M. et al., 2015, MNRAS, 449, 2604
Esteban C., Peimbert M., García-Rojas J., Ruiz M. T., Peimbert A., Rodríguez M., 2004, MNRAS, 355, 229
Esteban C., Méndez-Delgado J. E., García-Rojas J., Arellano-Córdova K. Z., 2022, ApJ, 931, 92
Fernandez M. A. et al., 2017, PASP, 129, 084201
Fischer W., Edwards S., Hillenbrand L., Kwan J., 2011, ApJ, 730, 73
Foster J. B. et al., 2015, ApJ, 799, 136
Gaia Collaboration, 2023, A&A, 674, A1
Gilmore G. et al., 2012, Messenger, 147, 25
Gray D. F., 2008, The Observation and Analysis of Stellar Photospheres. Cambridge Univ. Press, Cambridge
Grevesse N., Asplund M., Sauval A. J., 2007, Space Sci. Rev., 130, 105
Grilo V. et al., 2024, MNRAS, 534, 3005
Großschedl J. E., Alves J., Meingast S., Herbst-Kiss G., 2021, A&A, 647, A91
Guiglion G. et al., 2020, A&A, 644, A168
Gustafsson B., Edvardsson B., Eriksson K., Jørgensen U. G., Nordlund Å., Plez B., 2008, A&A, 486, 951
Hackshaw Z., Hawkins K., Filion C., Horta D., Laporte C. F. P., Carr C., Price-Whelan A. M., 2024, ApJ, 977, 143
Hawkins K., 2023, MNRAS, 525, 3318
Herczeg G. J., Hillenbrand L. A., 2014, ApJ, 786, 97
Hernández J. et al., 2023, AJ, 165, 205
Hinkel N. R., Timmes F. X., Young P. A., Pagano M. D., Turnbull M. C., 2014, AJ, 148, 54
Jönsson H. et al., 2020, AJ, 160, 120
Joy A. H., 1949, ApJ, 110, 424
Kollmeier J. A. et al., 2017, preprint (arXiv:1711.03234)
Kos J. et al., 2021, MNRAS, 506, 4232
Kos J. et al., 2025, preprint (arXiv:2501.06140)
Kounkel M. et al., 2018, AJ, 156, 84
Li G., Gordon I. E., Rothman L. S., Tan Y., Hu S.-M., Kassi S., Campargue A., Medvedev E. S., 2015, ApJS, 216, 15
Lodders K., 2003, ApJ, 591, 1220
Lodders K., Bergemann M., Palme H., 2025, Space Sci. Rev., 221, 23
López-Valdivia R. et al., 2024, MNRAS, 533, 395
Majewski S. R. et al., 2017, AJ, 154, 94
Marigo P. et al., 2017, ApJ, 835, 77
Martell S. L. et al., 2017, MNRAS, 465, 3203
Martinez-Medina L., Poggio E., Moreno-Hilario E., 2025, MNRAS, 542, L94
Masseron T., Merle T., Hawkins K., 2016. Astrophysics Source Code Library, record ascl:1605.004
Méndez-Delgado J. E., Amayo A., Arellano-Córdova K. Z., Esteban C., García-Rojas J., Carigi L., Delgado-Inglada G., 2022, MNRAS, 510, 4436
Méndez-Delgado J. E., Esteban C., García-Rojas J., Kreckel K., Peimbert M., 2023, Nature, 618, 249
Méndez-Delgado J. E., Esteban C., García-Rojas J., Kreckel K., Peimbert M., 2024a, Nat. Astron., 8, 275
Méndez-Delgado J. E. et al., 2024b, A&A, 690, A248
Muzerolle J., Calvet N., Hartmann L., D'Alessio P., 2003, ApJ, 597, L149
Natta A., Prusti T., Neri R., Wooden D., Grinin V. P., Mannings V., 2001, A&A, 371, 186
Neves V., Santos N. C., Sousa S. G., Correia A. C. M., Israelian G., 2009, A&A, 497, 563
Olander T., Heiter U., Kochukhov O., 2021, A&A, 649, A103
Olney R. et al., 2020, AJ, 159, 182
Osorio Y., Allende Prieto C., Hubeny I., Mészáros S., Shetrone M., 2020, A&A, 637, A80
Padgett D. L., 1996, ApJ, 471, 847
Pastorelli G. et al., 2020, MNRAS, 498, 3283
Peimbert M., 1967, ApJ, 150, 825
Plez B., 2012, Astrophysics Source Code Library, record ascl:1205.004
Poggio E. et al., 2022, A&A, 666, L4
Ritchey A. M., Jenkins E. B., Shull J. M., Savage B. D., Federman S. R., Lambert D. L., 2023, ApJ, 952, 57
Roman-Lopes A. et al., 2019, ApJ, 873, 66
Román-Zúñiga C. G. et al., 2023, AJ, 165, 51
Santos N. C., Melo C., James D. J., Gameiro J. F., Bouvier J., Gomes J. I., 2008, A&A, 480, 889
Simón-Díaz S., 2010, A&A, 510, A22
Sizemore L., Llanes D., Kounkel M., Hutchinson B., Stassun K., Chandra V., 2024, AJ, 167, 173
Smith V. V. et al., 2021, AJ, 161, 254
Sneden C., Lucatello S., Ram R. S., Brooke J. S. A., Bernath P., 2014, ApJS, 214, 26
Sprague D. et al., 2022, AJ, 163, 152
Stassun K. G., Mathieu R. D., Mazeh T., Vrba F. J., 1999, AJ, 117, 2941
Steinmetz M., 2003, in Munari U.ed., ASP Conf. Ser. Vol. 298, GAIA Spectroscopy: Science and Technology. Astron. Soc. Pac., San Francisco, p. 381
Tang J., Bressan A., Rosenfield P., Slemer A., Marigo P., Girardi L., Bianchi L., 2014, MNRAS, 445, 4287
Viana Almeida P., Santos N. C., Melo C., Ammler-von Eiff M., Torres C. A. O., Quast G. R., Gameiro J. F., Sterzik M., 2009, A&A, 501, 965
Walter D. K., Dufour R. J., Hester J. J., 1992, ApJ, 397, 196
Wright E. L. et al., 2010, AJ, 140, 1868
Zhao G., Zhao Y.-H., Chu Y.-Q., Jing Y.-P., Deng L.-C., 2012, Res. Astron. Astrophys., 12, 723
Zucker C., Speagle J. S., Schlafly E. F., Green G. M., Finkbeiner D. P., Goodman A., Alves J., 2020, A&A, 633, A51

## SUPPORTING INFORMATION

Supplementary data are available at *MNRAS* online.

**Tab2.mrt**

Please note: Oxford University Press is not responsible for the content or functionality of any supporting materials supplied by the authors. Any queries (other than missing material) should be directed to the corresponding author for the article.

[1]*Instituto de Astronomía, Universidad Nacional Autónoma de México, Ap. 106, Ensenada 22800, BC, México*
[2]*Universidad Católica del Norte, Instituto de Astronomía, Av. Angamos 0610, Antofagasta, Chile*
[3]*Facultad de Ciencias, Universidad Autónoma de Baja California, 22860 Ensenada, BC, México*
[4]*Instituto de Astronomía, Universidad Nacional Autónoma de México, Ap. 70-264, 04510 CDMX, México*
[5]*Department of Physics and Astronomy, University of North Florida, 1 UNF Dr, Jacksonville, FL 32224, USA*
[6]*Homer L. Dodge Department of Physics and Astronomy, University of Oklahoma, Norman, OK 73019, USA*
[7]*Centro de Investigación en Astronomía, Facultad de Ingeniería, Ciencia y Tecnología, Universidad Bernardo O'Higgins, Avenida Viel 1497, Santiago, Chile*
[8]*Department of Physics and Astronomy, Vanderbilt University, VU Station 1807, Nashville, TN 37235, USA*
[9]*Universidad Andres Bello, Facultad de Ciencias Exactas, Departamento de Física y Astronomía – Instituto de Astrofísica, Autopista Concepción-Talcahuano 7100, Talcahuano, Chile*
[10]*Steward Observatory, University of Arizona, 933 North Cherry Avenue, Tucson, AZ 85721-0065, USA*
[11]*Center for Astrophysics|Harvard & Smithsonian, 60 Garden Street, Cambridge MA 02138, USA*
[12]*Center for Astrophysics and Space Astronomy, University of Colorado Boulder, Boulder, CO 80309, USA*
[13]*Department of Astronomy, University of Virginia, Charlottesville, VA 2904, USA*
[14]*Department of Space, Earth & Environment, Chalmers University of Technology, E-412 96 Gothenburg, Sweden*
[15]*Departamento de Astronomía, Facultad de Ciencias – Universidad de La Serena, Av. Raul Bitran 1302, La Serena, Chile*
[16]*Instituto de Alta Investigación, Universidad de Tarapacá, Casilla 7D, Arica, Chile*
[17]*Universidad Nacional Autónoma de México, Instituto de Radioastronomía y Astrofísica, Antigua Carretera a Pátzcuaro 8701, Ex-Hda. San José de la Huerta, 58089 Morelia, Michoacán, México*

This paper has been typeset from a TEX/LATEX file prepared by the author.